Rotation of a spheroid in a Couette flow at moderate Reynolds numbers

Zhaosheng Yu
Department of Mechanics, Zhejiang University, Hangzhou 310027, China

Nhan Phan-Thien
Division of Bioengineering, National University of Singapore, Singapore 117576, Singapore

Roger I. Tanner
School of Aerospace, Mechanical and Mechatronic Engineering, University of Sydney, Sydney NSW 2006, Australia
(Received 28 March 2007; published 21 August 2007)

The rotation of a single spheroid in a planar Couette flow as a model for simple shear flow is numerically simulated with the distributed Lagrangian multiplier based fictitious domain method. The study is focused on the effects of inertia on the orbital behavior of prolate and oblate spheroids. The numerical orbits are found to be well described by a simple empirical model, which states that the rate of the spheroid rotation about the vorticity axis is a sinusoidal function of the corresponding projection angle in the flow-gradient plane, and that the exponential growth rate of the orbit function is a constant. The following transitions in the steady state with increasing Reynolds number are identified: Jeffery orbit, tumbling, quasi-Jeffery orbit, log rolling, and inclined rolling for a prolate spheroid; and Jeffery orbit, log rolling, inclined rolling, and motionless state for an oblate spheroid. In addition, it is shown that the orbit behavior is sensitive to the initial orientation in the case of strong inertia and there exist different steady states for certain shear Reynolds number regimes.

DOI: 10.1103/PhysRevE.76.026310 PACS number(s): 47.15.−x

I. INTRODUCTION

The suspension of nonspherical particles is commonly encountered in engineering applications and the particle orientations are important to the macroscopic behavior of the suspensions. Therefore, the particle orientation has been a subject of extensive investigations. Jeffery [1] analyzed the motion of an ellipsoid theoretically in a simple shear flow at zero Reynolds number, and found that the ellipsoid rotated about the vorticity axis (perpendicular to the flow-gradient plane) along a closed orbit, dependent solely on the initial condition. Bretherton [2] extended Jeffery's solution to encompass all axisymmetric particles by simply replacing the aspect ratio of particles with an effective aspect ratio. Using asymptotic methods, Harper and Chang [3] showed that the trajectories of a three-dimensional (3D) spheroid will be a periodic orbit which corresponds to maximum dissipation.

When the effect of fluid elasticity is present, theories [4,5], experiments [6], and numerical simulations [7] revealed that the axis of a fiber (or a prolate spheroid) spiraled towards the vorticity axis in a weakly elastic fluid. However, in a highly elastic fluid, the final fixed orientation was along the flow direction [8].

When the effect of weak fluid inertia is present, both the theory [9] and experiments [10] revealed that the axis of a prolate spheroid gradually turned into the flow-gradient plane, whereas an oblate spheroid eventually aligned its axis of symmetry with the vorticity axis. Feng and Joseph [11] numerically investigated the rotation of an ellipsoid in a simple shear flow and discussed the deviation of the particle motion from the Jeffery orbit due to particle and fluid inertia. Broday *et al.* [12] examined the motion of spheroid particles in a vertical shear flow, with emphasis on the effects of fluid inertia on the particle migration across streamlines. In these two numerical works, the Reynolds numbers are relatively small.

Ding and Aidun [13] investigated numerically the effect of strong fluid inertia on the dynamics of an elliptical cylinder and an ellipsoid suspended in shear flow with the lattice Boltzmann method. The rotational motion was confined to the flow-gradient plane and they found that the angular velocity of the particle decreased with increasing Reynolds number and the rotation stopped when the Reynolds number exceeded a critical value. They found that the rotation period scaled as $(\mathrm{Re}_c-\mathrm{Re})^{-1/2}$ near the transitional point; here Re_c and Re are the critical Reynolds number and the Reynolds number. Zettner and Yoda [14] studied experimentally the effects of fluids inertia, geometry, and flow confinement upon the dynamics of neutrally buoyant elliptical cylinders over a wide range of aspect ratios in simple shear flow at moderate shear Reynolds numbers, and the results confirmed that an elliptical cylinder of moderate aspect ratio ceases to rotate, resting at a nearly horizontal equilibrium orientation above a critical Reynolds number. The experiment also supported the scaling of $(\mathrm{Re}_c-\mathrm{Re})^{-1/2}$.

Qi and Luo [15,16] reported some numerical results about the three-dimensional rotations of a spheroid in Couette flow at moderate Reynolds numbers. Their investigations were focused on the transitions in the steady state with increasing Re. They identified three Re regimes for a prolate spheroid: at low Re, the particle tumbled in the flow-gradient plane, as observed previously by Karnis *et al.* [10]; at intermediate Re, the axis of the spheroid deviated from the flow gradient, i.e., $0<\theta<\pi/2$, and at higher Re, the spheroid rolled with its axis parallel to the vorticity axis, i.e., $\theta=0$. Here, θ denotes the angle between the orientation of the prolate spheroid and the vorticity axis (see Fig. 1). For an oblate spheroid, "rolling" about the vorticity axis at relatively low Re and "inclined rolling" at higher Re were identified. The results of Qi and Luo [15,16] enhance greatly the understanding of the

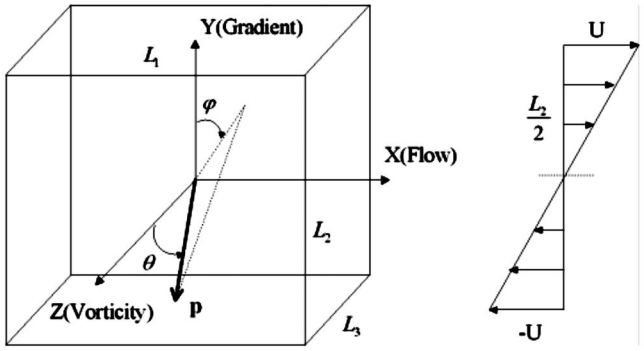

FIG. 1. Schematic diagram of a spheroid rotating in Couette flow. The computational domain is a box with the size of $L_1 \times L_2 \times L_3$. Periodic boundary conditions are introduced in the streamwise (X) and spanwise (Z) directions. Note that the definition of φ in this paper may differ from the definition in some of the literature.

rotational and orientational behavior of a spheroid particle in linear shear flow at moderate Reynolds numbers. However, in their simulations, the rotation period of a spheroid did not increase significantly with increasing Reynolds number and an oblate spheroid never ceased to rotate, which are inconsistent with the observations of Ding and Aidun [13], and Zettner and Yoda [14].

In the present study, we reexamine the rotation behavior of both prolate and oblate spheroids in Couette flow at moderate Reynolds numbers using the distributed Lagrangian multiplier based fictitious domain (DLM/FD) method [17,18]. Our results are consistent with the observations of Ding and Aidun [13], and Zettner and Yoda [14]. The reason for the discrepancies between our results and those of Qi and Luo (apart from the methodologies) is not known. In addition, we propose a simple empirical model for the prediction of the rotation of a spheroid in simple shear flow, which is described in the next section. In Sec. III, the numerical method is presented. We then report and discuss the results for the prolate and oblate cases, respectively. The concluding remarks will be given in the final section.

II. PRELIMINARIES

A. Jeffery orbit

In a simple shear flow, a prolate spheroid rotates in a Jeffery orbit, described by

$$\dot{\mathbf{p}} = (\mathbf{I} - \mathbf{pp}) \cdot \tilde{\mathbf{L}} \cdot \mathbf{p}, \tag{1}$$

where $\mathbf{p}$ is a unit vector along the symmetry axis of the spheroid, $\tilde{\mathbf{L}}$ is the effective velocity gradient tensor

$$\tilde{\mathbf{L}} = \mathbf{L} - \zeta \mathbf{D}, \tag{2}$$

in which $\mathbf{L}=\nabla \mathbf{u}^T$ is the velocity gradient tensor, $\mathbf{u}$ is the velocity vector, $\mathbf{D}=(\mathbf{L}+\mathbf{L}^T)/2$ is the strain rate tensor, and $\zeta=2/(a_r^2+1)$, where a_r is the aspect ratio (major diameter/minor diameter) of the spheroid.

Define θ as the angle between $\mathbf{p}$ and the vorticity (Z) axis, and φ as the angle between the projection of $\mathbf{p}$ on the (X,Y) plane and the Y axis (see Fig. 1), so that

$$p_x = \sin\theta \sin\varphi, \quad p_y = \sin\theta \cos\varphi, \quad p_z = \cos\theta. \tag{3}$$

The solution to the Jeffery equation is

$$\tan\varphi = a_r \tan(\omega t + k'), \quad \tan\theta = \frac{Ca_r}{\sqrt{a_r^2 \cos^2\varphi + \sin^2\varphi}}, \tag{4}$$

where $\omega=2\pi/T$, $T=2\pi(a_r+a_r^{-1})/\dot{\gamma}$ is the orbit period, here $\dot{\gamma}$ is the shear rate of the flow. The constants k' and C are determined from the initial orientation φ_0 and θ_0.

B. An empirical model for a general orbit

To account for the effects of inertia, we suppose that the motion of the spheroid is still approximated by Jeffery's equation (1), but with the "effective" velocity gradient tensor

$$\tilde{\mathbf{L}} = \begin{pmatrix} 0 & a'\dot{\gamma} & 0 \\ -b'\dot{\gamma} & 0 & 0 \\ 0 & 0 & -c'\dot{\gamma} \end{pmatrix}, \tag{5}$$

where a', b', and c' are some constants to be identified using numerical data. The solution to (1) is

$$\mathbf{p} = \mathbf{Q}/Q,$$

$$Q_x = \sqrt{a'/b'} B_0 \sin(\omega t + k'), \quad Q_y = B_0 \cos(\omega t + k'), \quad Q_z = Q_{z0} e^{-c'\dot{\gamma}t}, \tag{6}$$

where $\omega=\sqrt{a'b'}\dot{\gamma}$, and B_0 and k' are two constants related to the initial orientation of the spheroid, $B_0=\sqrt{Q_{y0}^2+(b'/a')Q_{x0}^2}$ and $\tan(k')=\sqrt{b'/a'}Q_{x0}/Q_{y0} = \sqrt{b'/a'}\tan\varphi_0$.

To characterize the general orbit, we define an orbit function $C(t)$ by

$$C(t) = a_r^{-1} \tan\theta(t) \sqrt{a_r^2 \cos^2\varphi(t) + \sin^2\varphi(t)}, \tag{7}$$

so that $C(t)$ is a constant for the Jeffery orbit. From (7), it is clear that $\tan\theta=C$ at $\varphi=m\pi$ (m being an integer) and $\tan\theta = a_r C$ at $\varphi=m\pi+\pi/2$. In light of (3), Eq. (7) can be rewritten as

$$C(t) = \frac{\sqrt{a_r^2 p_y^2 + p_x^2}}{a_r |p_z|}. \tag{8}$$

To extract the exponential growth rate in $C(t)$, we define another orbit function

$$G(t) = \ln C(t). \tag{9}$$

With the "effective" velocity gradient tensor, it is possible for one to establish the constitutive equations of fiber suspensions that account for the effects of fluid inertia or elasticity [19,20].

1. Behavior of the orbit predicted by the model about φ

From Eq. (6) and $\tan\varphi=Q_x/Q_y$, one obtains

$$\tan\varphi = \sqrt{a'/b'}\,\tan(\omega t + k'). \tag{10}$$

Taking the time derivative of (10) yields

$$\dot{\varphi} = (a'\cos^2\varphi + b'\sin^2\varphi)\dot{\gamma} = \left(\frac{a'+b'}{2} + \frac{a'-b'}{2}\cos 2\varphi\right)\dot{\gamma}, \tag{11}$$

which means that $\dot{\varphi}$ is a cosine function of φ with period π, average value $\frac{a'+b'}{2}\dot{\gamma}$, and amplitude $\frac{a'-b'}{2}\dot{\gamma}$. For a prolate (oblate) spheroid, $\dot{\varphi}$ reaches its maximum (minimum) $a'\dot{\gamma}$ at $\varphi = m\pi$ and its minimum (maximum) $b'\dot{\gamma}$ at $\varphi = m\pi + \pi/2$.

2. Behavior of the orbit predicted by the model: about G

From Eq. (6), we have

$$Q_x\left(t+\frac{T}{4}\right) = \sqrt{\frac{a'}{b'}}Q_y(t), \quad Q_y\left(t+\frac{T}{4}\right) = -\sqrt{\frac{b'}{a'}}Q_x(t),$$

$$Q_z\left(t+\frac{T}{4}\right) = Q_z(t)e^{-c'\dot{\gamma}(T/4)}. \tag{12}$$

Then, recalling the definition of C given in (8), one obtains

$$\frac{C\left(t+\frac{T}{4}\right)}{C(t)} = \frac{\sqrt{a_r^2(b'/a')Q_x^2(t) + (a'/b')Q_y^2(t)}}{\sqrt{a_r^2Q_y^2(t) + Q_x^2(t)}}e^{c'\dot{\gamma}(T/4)}. \tag{13}$$

For $t=t_1$ when $\varphi = m\pi$ (m being an integer), i.e., $Q_x = 0$,

$$\frac{C\left(t_1+\frac{T}{4}\right)}{C(t_1)} = \frac{1}{a_r}\sqrt{\frac{a'}{b'}}e^{c'\dot{\gamma}(T/4)}, \tag{14}$$

$$G\left(t_1+\frac{T}{4}\right) = G(t_1) + c'\frac{\dot{\gamma}T}{4} + \ln\sqrt{\frac{a'}{b'}} - \ln a_r. \tag{15}$$

For $t=t_2$ when $\varphi = m\pi + \pi/2$, i.e., $Q_y = 0$,

$$\frac{C\left(t_2+\frac{T}{4}\right)}{C(t_2)} = a_r\sqrt{\frac{b'}{a'}}e^{c'\dot{\gamma}(T/4)}, \tag{16}$$

$$G\left(t_2+\frac{T}{4}\right) = G(t_2) + c'\frac{\dot{\gamma}T}{4} - \left(\ln\sqrt{\frac{a'}{b'}} - \ln a_r\right). \tag{17}$$

Equations (15) and (17) imply

$$G|_{\varphi=(m+1)\pi} - G|_{\varphi=m\pi} = G|_{\varphi=m\pi+\pi/2} - G|_{\varphi=m\pi-\pi/2} = c'\frac{\dot{\gamma}T}{2}.$$

Define

$$A = \ln\sqrt{\frac{a'}{b'}} - \ln a_r. \tag{18}$$

A denotes the average amplitude of $G(t)$. $G(t)$ can be regarded as a combination of a periodic function with period $T/2$, amplitude A and a linear function of slope $c'\dot{\gamma}$. Given A and T, a' and b' can be solved,

$$a' = \frac{2\pi a_r}{T\dot{\gamma}}e^{A}, \quad b' = \frac{2\pi}{T\dot{\gamma}a_r}e^{-A}. \tag{19}$$

The Jeffery orbit is recovered at $a' = a_r^2/(1+a_r^2)$, $b' = 1/(1+a_r^2)$, and $c' = 0$.

C. Numerical method

The DLM/FD method developed by Glowinski *et al.* [17] is employed here to numerically simulate the motion of the spheroid. Consider a particle with density ρ_d moving in a Newtonian fluid with density ρ_l and solvent viscosity η. By introducing the scales L_c for length, U_c for velocity, L_c/U_c for time, $\rho_l U_c^2$ for pressure, $\rho_l U_c^2/L_c$ for the distributed Lagrange multiplier, $\rho_d L_c^3$ for mass, and $\rho_d L_c^5$ for moment of inertia, the dimensionless weak formulation of the governing equations in the case of Dirichlet (or periodic) boundary condition is stated as follows.

For $t>0$, *find* $\mathbf{u} \in W_{\mathbf{u}\Gamma}$, $p \in L_0^2(\Omega)$, $\boldsymbol{\lambda} \in \Lambda(t)$, $\mathbf{U} \in R^3$, *and* $\boldsymbol{\omega} \in R^3$ *satisfying* the following:

(1) *combined momentum equation*,

$$\int_\Omega \left(\frac{\partial \mathbf{u}}{\partial t} + \mathbf{u}\cdot\nabla\mathbf{u}\right)\cdot\mathbf{v}d\mathbf{x} - \int_\Omega p\,\nabla\cdot\mathbf{v}d\mathbf{x} + \frac{1}{\mathrm{Re}}\int_\Omega (\nabla\mathbf{u})^T{:}\nabla\mathbf{v}d\mathbf{x} + (\rho_r - 1)\left[M\left(\frac{d\mathbf{U}}{dt} - \mathrm{Fr}\frac{\mathbf{g}}{g}\right)\cdot\mathbf{V} + \frac{d(\mathbf{J}\cdot\boldsymbol{\omega})}{dt}\cdot\boldsymbol{\xi}\right] = \langle\boldsymbol{\lambda}, \mathbf{v} - (\mathbf{V} + \boldsymbol{\xi}\times\mathbf{r})\rangle_{P(t)}$$

for all $\mathbf{v} \in W_0(t)$, $\mathbf{V} \in R^3$, $\boldsymbol{\xi} \in R^3$; (20)

(2) *incompressibility constraint*,

$$\int_\Omega q\,\nabla\cdot\mathbf{u}d\mathbf{x} = 0 \quad \text{for all } q \in L^2(\Omega); \tag{21}$$

(3) *rigid-body motion constraint inside (and on) the particle boundary*,

$$\langle\boldsymbol{\mu}, \mathbf{u} - (\mathbf{U} + \boldsymbol{\omega}\times\mathbf{r})\rangle_{P(t)} = \mathbf{0} \quad \text{for all } \boldsymbol{\mu} \in \Lambda(t), \tag{22}$$

(4) *and kinematic equations of the particle*,

$$\frac{d\mathbf{X}}{dt} = \mathbf{U}, \tag{23}$$

$$\begin{pmatrix}\dot{q}_1\\ \dot{q}_2\\ \dot{q}_3\\ \dot{q}_4\end{pmatrix} = \frac{1}{2}\begin{pmatrix} q_4 & -q_3 & q_2 & q_1\\ q_3 & q_4 & -q_1 & q_2\\ -q_2 & q_1 & q_4 & q_3\\ -q_1 & -q_2 & -q_3 & q_4\end{pmatrix}\begin{pmatrix}\omega_x\\ \omega_y\\ \omega_z\\ 0\end{pmatrix}. \tag{24}$$

Here, $\mathbf{u}$, p, $\mathbf{U}$, $\boldsymbol{\omega}$, and λ are the fluid velocity, pressure, particle translational and angular velocities, and the distributed Lagrange multiplier, respectively, and $\mathbf{v}$, q, $\mathbf{V}$, $\boldsymbol{\xi}$, and $\boldsymbol{\mu}$ are their corresponding variations. M and $\mathbf{J}$ are the mass and the moment of inertia of the particle, respectively. $\mathbf{r}$ is the position vector with respect to the center of the particle $\mathbf{X}$, and $\mathbf{g}$ is the acceleration of gravity. In the above equations,

the following dimensionless parameters are introduced:

Physical parameters,

$$\text{density ratio } \rho_r = \rho_d/\rho_l. \tag{25}$$

Dynamic parameters,

$$\text{Reynolds number Re} = \frac{\rho_l U_c L_c}{\eta}, \tag{26}$$

$$\text{Froude number Fr} = \frac{g L_c}{U_c}. \tag{27}$$

Here the Froude number represents the relative importance of gravity to inertia. The following variation spaces are used:

$$W_{\mathbf{u}\Gamma} = \{\mathbf{v} \in H^1(\Omega)^3 | \mathbf{v} = \mathbf{u}_\Gamma(t) \text{ on } \Gamma\},$$

$$W_0 = \{\mathbf{v} \in H^1(\Omega)^3 | \mathbf{v} = \mathbf{0} \text{ on } \Gamma\},$$

$$L_0^2 = \left\{ q \in L^2(\Omega) \middle| \int_\Omega q d\mathbf{x} = 0 \right\}, \tag{28}$$

and $\Lambda(t)$ is an appropriate space by which the constraint of rigid-body motion in $P(t)$ is enforced. The angle brackets denote an inner product defined in $\Lambda(t)$. $P(t)$ signifies the region inside and including the particle boundary, Ω is the entire computational domain including both the particle's interior and exterior, and Γ is the boundary of Ω.

In (24), q_1, q_2, q_3, q_4 are the components of a quaternion, which can be defined in terms of the Euler angles [21],

$$q_1 = \sin(\theta/2)\cos[(\phi - \psi)/2], \quad q_2 = \sin(\theta/2)\sin[(\phi - \psi)/2],$$

$$q_3 = \cos(\theta/2)\sin[(\phi + \psi)/2], \quad q_4 = \cos(\theta/2)\cos[(\phi + \psi)/2]. \tag{29}$$

The components are normalized, $\Sigma_m q_m^2 = 1$, ω_x, ω_y, and ω_z in (24) represent the components of the angular velocity measured in a body-fixed frame. Both the quaternion and the Euler angles can describe the relationship between the body-fixed frame and the space-fixed frame. However, the Euler angles themselves cannot be determined unambiguously at $\sin\theta = 0$, and consequently are not employed here. With the quaternion, the coordinate transformation matrix from the space-fixed frame to the body-fixed frame is

$$\mathbf{A} = 2\begin{pmatrix} q_1^2 + q_4^2 - \frac{1}{2} & q_1 q_2 + q_3 q_4 & q_1 q_3 - q_2 q_4 \\ q_1 q_2 - q_3 q_4 & q_2^2 + q_4^2 - \frac{1}{2} & q_2 q_3 + q_1 q_4 \\ q_1 q_3 + q_2 q_4 & q_2 q_3 - q_1 q_4 & q_3^2 + q_4^2 - \frac{1}{2} \end{pmatrix}. \tag{30}$$

Note that A is an orthogonal matrix. For an axisymmetric body such as a spheroid, z axis of a body-fixed frame alone is able to determine the orientation of the body, and that is $(\sin\phi\sin\theta, -\cos\phi\sin\theta, \cos\theta)$, or $2(q_1 q_3 + q_2 q_4, q_2 q_3 - q_1 q_4, q_3^2 + q_4^2 - \frac{1}{2})$ in the space-fixed frame.

D. Computational scheme

The operator-splitting technique proposed by Glowinski *et al.* [17] is used to decompose the system (20)–(22) into some subsystems. The essential step is to divide the original fluid-solid system into a fluid-flow part and a particle-motion part in the following forms:

(1) Fluid-flow part, find $\mathbf{u}^\# \in W_{\mathbf{u}\Gamma}$, $p \in L_0^2(\Omega)$, satisfying

$$\int_\Omega \left(\frac{\mathbf{u}^\# - \mathbf{u}^n}{\Delta t} + \mathbf{u}^n \cdot \nabla \mathbf{u}^n \right) \cdot \mathbf{v} d\mathbf{x} - \int_\Omega p \nabla \cdot \mathbf{v} d\mathbf{x} + \frac{1}{\mathrm{Re}} \int_\Omega (\nabla \mathbf{u}^{n+1})^T : \nabla \mathbf{v}^{n+1} d\mathbf{x} = 0 \quad \text{for all } \mathbf{v} \in W_0(t), \tag{31}$$

$$\int_\Omega q \nabla \cdot \mathbf{u}^\# d\mathbf{x} = 0 \quad \text{for all } q \in L^2. \tag{32}$$

(2) Particle-motion part, find $\mathbf{u}^{n+1} \in W_{\mathbf{u}\Gamma}$, $\boldsymbol{\lambda} \in \Lambda(t)$, $\mathbf{U}^{n+1} \in R^3$, and $\boldsymbol{\omega}^{n+1} \in R^3$ satisfying

$$\int_\Omega \left(\frac{\mathbf{u}^{n+1} - \mathbf{u}^\#}{\Delta t} \right) \cdot \mathbf{v} d\mathbf{x} + (\rho_r - 1) \left[M \left(\frac{\mathbf{U}^{n+1} - \mathbf{U}^n}{\Delta t} - \mathrm{Fr} \frac{\mathbf{g}}{g} \right) \right] \cdot \mathbf{V} + (\rho_r - 1) \left(\frac{\mathbf{J} \cdot (\boldsymbol{\omega}^{n+1} - \boldsymbol{\omega}^n)}{\Delta t} + \boldsymbol{\omega}^n \times (\mathbf{J} \cdot \boldsymbol{\omega}^n) \right) \cdot \boldsymbol{\xi} = \langle \boldsymbol{\lambda}, \mathbf{v} - (\mathbf{V} + \boldsymbol{\xi} \times \mathbf{r}) \rangle_{P^n},$$

$$\text{for all } \mathbf{v} \in W_0,\ \mathbf{V} \in R^3,\ \boldsymbol{\xi} \in R^3, \tag{33}$$

$$\langle \boldsymbol{\mu}, \mathbf{u}^{n+1} - (\mathbf{U}^{n+1} + \boldsymbol{\omega}^{n+1} \times \mathbf{r}) \rangle_{P^n} = 0 \quad \text{for all } \boldsymbol{\mu} \in \Lambda(t), \tag{34}$$

and then determine $\mathbf{X}^{n+1}$ and q_i^{n+1} by integrating (23) and (24).

It was found that the finite difference method can be used to solve the above subproblems as a substitute of the finite element method [18]. Here, the projection method and the alternating direction implicit (ADI) technique [18] are used to solve the fluid-flow subproblem. The second part above (33) and (34) is a saddle-point problem and can be solved with the conjugate gradient method [17]. The collocation point method is employed to discretize the distributed Lagrange multiplier for a spheroid. The control points are located in a sequence of evenly distributed parallel planes that are perpendicular to the axis of symmetry of the spheroid and their distribution in each plane has the same pattern as devised by Yu *et al.* [22]. The distance between neighboring control points are slightly coarser than the velocity mesh size. In our implementation, the fluid velocity $\mathbf{u}$, the particle translational velocity $\mathbf{U}$, and the Lagrange multiplier $\boldsymbol{\lambda}$ are measured in the space-fixed frame, while the particle angular velocity $\boldsymbol{\omega}$ and the position vector $\mathbf{r}$ are measured in the body-fixed frame. Therefore, three coordinate transformations are required for solving (33) and (34): one is for determining $P: \mathbf{x} = \mathbf{X} + \mathbf{A}^{-1} \cdot r$; one is to transform $\boldsymbol{\lambda}$ from the space-fixed frame to the body-fixed frame when dealing with the angular velocity component equation in (33); and the last one is to transform $\boldsymbol{\omega} \times \mathbf{r}$ from the body-fixed frame to the space-fixed frame in (34). The reader is referred to [23] for a more detailed description of the algorithm.

The schematic diagram of the flow is given in Fig. 1. The computational domain is a box of sizes $L_1 \times L_2 \times L_3$. Periodic boundary conditions are introduced in the streamwise (X) and spanwise (Z) directions. The top and bottom plates move with velocity U and $-U$, respectively. We consider a spheroid of the symmetry axis length $2a$ and the equatorial diameter $2b$. U and $L_2/2$ are taken as the characteristic velocity and the characteristic length, respectively. Thus, a time scale is $1/\dot{\gamma}$ and the Reynolds number is defined by $\mathrm{Re} = \rho_l U L_2/(2\eta)$.

We set $\rho_r = 1.001$ and $\mathrm{Fr} = 0$, as an approximation to the neutrally buoyant case. Such an approximation has been demonstrated to be excellent [18]. Actually, it is impossible to encounter a perfectly neutrally buoyant case in practice. The dimensionless control parameters are as follows:

$$\text{spheroid aspect ratio,} \quad a_r = \frac{a}{b}; \tag{35}$$

$$\text{confinement ratio,} \quad \begin{cases} \lambda_a = \dfrac{2a}{L_2} & \text{for a prolate spheroid,} \\ \lambda_b = \dfrac{2b}{L_2} & \text{for an oblate spheroid;} \end{cases} \tag{36}$$

shear Reynolds number,

$$\begin{cases} \mathrm{Re}_s = \dfrac{\rho_l 4a^2\dot{\gamma}}{\eta} = 4\lambda_a^2\,\mathrm{Re} & \text{for a prolate spheroid,} \\ \mathrm{Re}_s = \dfrac{\rho_l 4b^2\dot{\gamma}}{\eta} = 4\lambda_b^2\,\mathrm{Re} & \text{for an oblate spheroid.} \end{cases} \tag{37}$$

In addition, because we adopt periodic boundary conditions, the flow fields are also affected by L_1 and L_3. For convenience, we will use L_1 and L_3 to represent the corresponding dimensionless quantities. Throughout this study, we set $L_1 = L_2 = 2$ (i.e., a cubic domain), $a_r = 2$ and $\lambda_a = 0.4$ for a prolate spheroid, and $a_r = 0.5$ and $\lambda_b = 0.4$ for an oblate spheroid. We note that the results are not sensitive to the increase in the size of box at a relatively low Reynolds number. We focus on the effects of inertia in the present study, and postpone the effects of other factors such as the interactions between neighboring spheroids and the fluid viscoelasticity to future works. The spheroid is released at the center of the computation domain with zero velocities. Although we did not impose any constraints for the translational motion of the spheroid, the departure of the spheroid center away from the initial position was found negligible for all cases studied. The spatial resolution is $64 \times 64 \times 64$, and the time step is 0.005 or 0.01.

III. RESULTS AND DISCUSSION

A. Validation of the numerical method

To validate our numerical method, we compare the calculated orientational orbits for a prolate spheroid and the analytical Jeffery orbits in Fig. 2 at a low Reynolds number for $a_r = 2$ and 3, respectively. For our computations, $\mathrm{Re}_s = 0.5$, $h = b/6.4$, $\Delta t = 0.001$, $\varphi_0 = \pi/2$, and $\theta_0 = \pi/4$. The two results are in remarkably good agreement with each other.

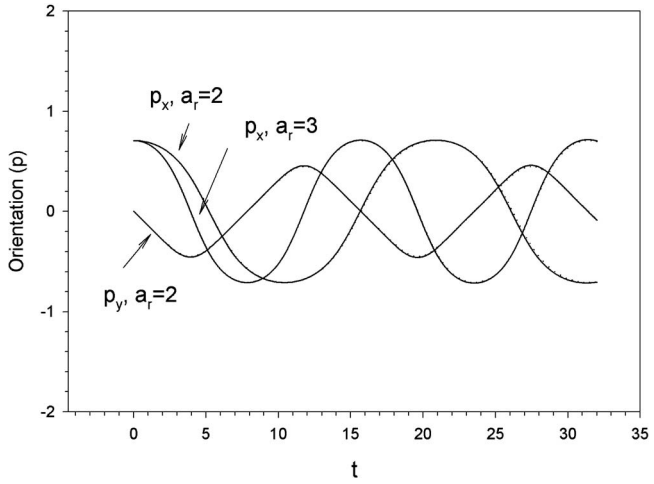

FIG. 2. Comparison between the calculated orientational orbit and the analytical Jeffery orbit for a prolate spheroid in simple shear flow at a low Reynolds number. Solid lines, our results; dotted lines, analytical results, the two being in excellent agreement.

There are no data available for the comparison in the case of 3D and high Reynolds numbers. Therefore, we perform a convergence test for the case of $\mathrm{Re}_s = 128$, $\theta_0 = \frac{\pi}{6}$, and $\varphi_0 = \frac{\pi}{2}$, and the results are presented in Fig. 3. The computations at high Reynolds numbers are more difficult than at low Reynolds numbers, and therefore the accuracy of the computational results at high Re appears less accurate compared to the case of low Re. Nevertheless, the results obtained with the mesh of $(64 \times 64 \times 64)$ and the time step of 0.01 converge reasonably well.

We will analyze the orbit behavior of a spheroid through the projected rotation angle in the flow-gradient plane $\varphi(t)$ and the orbit function $G(t)$. $\varphi(t)$ reflects the behavior of p_x and p_y, and $G(t)$ contains the information about p_z. Given φ and G, p_x, p_y, and p_z are uniquely determined.

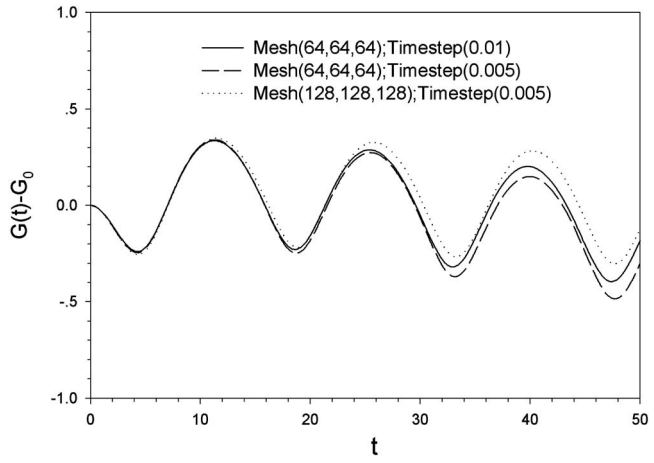

FIG. 3. Convergence test at $\mathrm{Re}_s = 128$, $\theta_0 = \frac{\pi}{6}$, and $\varphi_0 = \frac{\pi}{2}$.

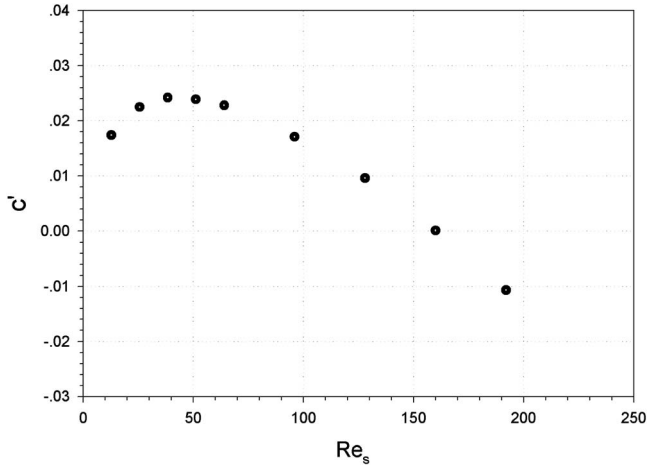

FIG. 4. The growth rate c' vs Re_s for a prolate spheroid calculated from the data for $\varphi=\frac{3\pi}{2}-\frac{5\pi}{2}$. $\theta_0=\frac{\pi}{4}$, $\varphi_0=\frac{\pi}{2}$.

B. Prolate case

1. Orbit behavior at different Re

We examine the orbit behavior at a fixed initial orientation of $\theta_0=\frac{\pi}{4}$ and $\varphi_0=\frac{\pi}{2}$. For $\mathrm{Re}_s=0-256$, our numerical results indicate that there exist two critical shear Reynolds numbers and thereby three Reynolds regimes:

(i) $\mathrm{Re}_s=0$. The spheroid rotates according to the Jeffery orbit (4). $G(t)$ is a constant and $\dot{\varphi}$ is a cosine function of φ with the maximum of 0.8 and the minimum of 0.2 for $a_r=2$.

(ii) Regime one ($0<\mathrm{Re}_s<\mathrm{Re}_{sc1}\approx 160$). Figure 4 reveals that c', the exponential growth rate of the orbit constant $C(t)$, is positive, i.e., the prolate spheroid will eventually turn its axis of symmetry into the flow-gradient plane. More precisely, our results show that c' is an increasing function of time or $G(t)$, and this is more obvious at higher Re_s (Fig. 5). Thus, we compute c' only from $G(t)$ at $\varphi=\frac{3\pi}{2}-\frac{5\pi}{2}$ for an overview of the relationship between c' and Re_s (Fig. 4),

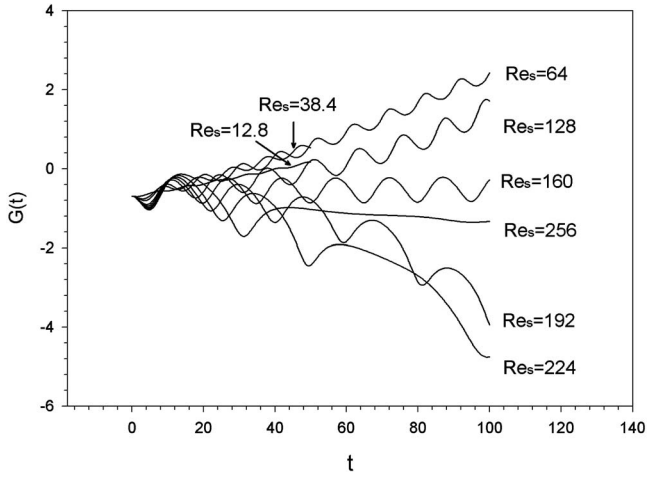

FIG. 5. The evolutions of the orbit function G at different Re_s. $\theta_0=\frac{\pi}{4}$, $\varphi_0=\frac{\pi}{2}$.

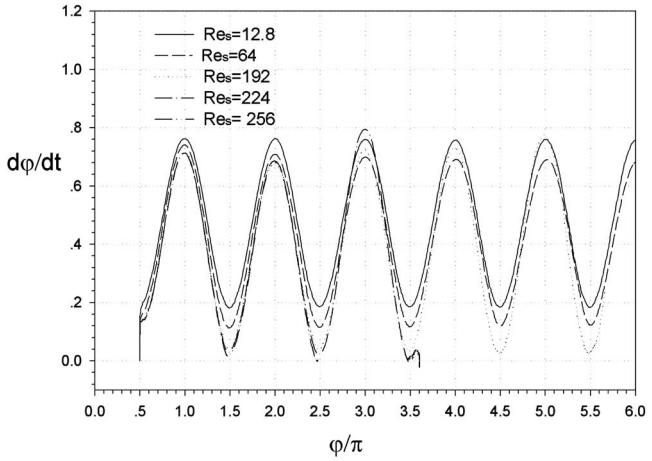

FIG. 6. $(d\varphi/dt)$ vs φ/π at different Re_s for a prolate spheroid. $\theta_0=\frac{\pi}{4}$, $\varphi_0=\frac{\pi}{2}$.

from which we can see that c' reaches its maximum at $\mathrm{Re}_s\approx 40$. These results are in qualitative agreement with the experiments of Karnis *et al.* [10] in which they investigated the behavior of $G(t)$ at low Re_s, and observed that c' was approximately a constant with time; its slope (with respect to Re_s) was a decreasing function of Re_s. Figure 6 shows that $\dot{\varphi}$ is a cosinelike function of φ. A further analysis of the behavior of $\varphi(t)$ will be presented later.

(iii) $\mathrm{Re}_s=\mathrm{Re}_{sc1}\approx 160$. $G(t)$ is a periodic function with zero growth rate, i.e., $c'=0$.

(iv) Regime two ($\mathrm{Re}_{sc1}<\mathrm{Re}_s\leqslant\mathrm{Re}_{sc2}$). In this regime, the spheroid will turn its axis parallel to the vorticity axis, i.e., $c'<0$. From Fig. 5, the second critical shear Reynolds number Re_{sc2} is between 224 and 256. At the end of the simulation, the spheroid at $\mathrm{Re}_s=192$ is still rotating periodically about the vorticity axis (Figs. 5 and 6), whereas, the spheroid at $\mathrm{Re}_s=224$ almost ceases the rotation, staying in the vicinity of the flow-vorticity plane (Figs. 6 and 7), but continues its approach to the vorticity axis. In this case, the calculations of φ and G cannot be quantitatively accurate due to two diffi-

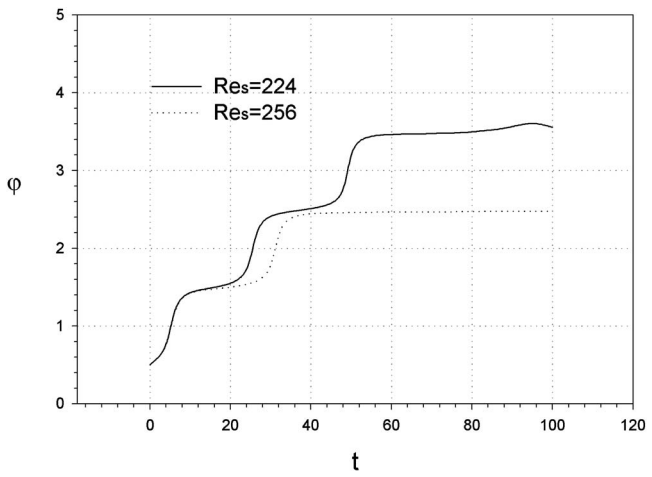

FIG. 7. The evolutions of φ in cases where the rotation about the vorticity axis of the spheroid stops. $\theta_0=\frac{\pi}{4}$, $\varphi_0=\frac{\pi}{2}$.

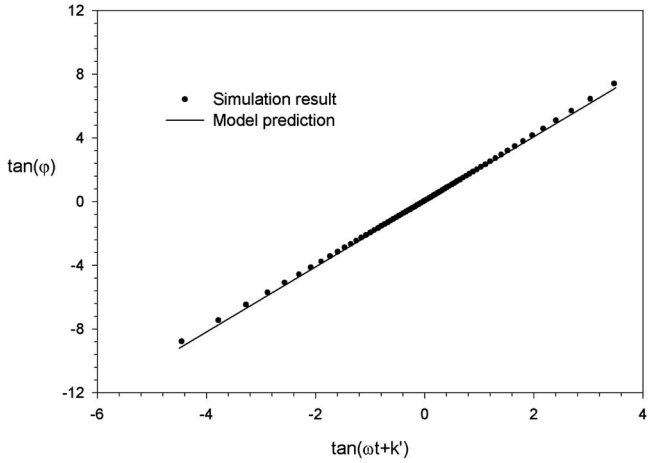

FIG. 8. $\tan(\varphi)$ vs $\tan(\omega t+k')$ at $\mathrm{Re}_s=12.8$, as compared to the model prediction. For the simulation result, $T=16.6$, and for the model prediction, $a'=0.762$, $b'=0.182$.

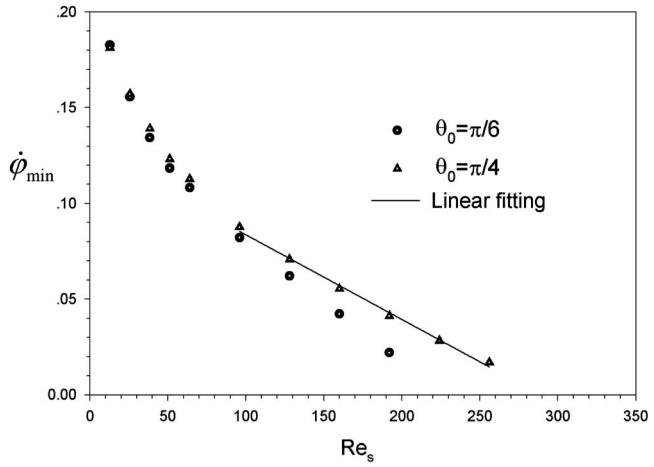

FIG. 9. $(d\varphi/dt)_{\min}$ vs Re_s for $\theta_0=\frac{\pi}{6}$ and $\theta_0=\frac{\pi}{4}$. The linear fitting function is $(d\varphi/dt)_{\min}=4.424\times10^{-4}(289-\mathrm{Re}_s)$. $\varphi_0=\frac{\pi}{2}$.

culties: one is that the minimum of $\dot{\varphi}$ is small and the other is that the axis of the spheroid approaches very close to the vorticity axis. There is no meaningful definition for φ when the two axes coincide exactly.

(v) Regime three ($\mathrm{Re}_s>\mathrm{Re}_{sc2}$). As Re_s increases above Re_{sc2}, the vorticity axis is no longer the stable attractor, and the spheroid stays in almost the flow-vorticity plane with θ between 0 and $\frac{\pi}{2}$ (Figs. 5–7). Since the spheroid never stops its spin about its axis unless it turns into the flow-gradient plane, we call the motion "inclined rolling," the term used by Qi and Luo [15,16].

With the shear Reynolds number increasing from zero to 256, the particle's rotation undergoes the following transitions: Jeffery orbit, tumbling, quasi-Jeffery orbit, log rolling, and inclined rolling.

2. Assessment of the model

We observed that both φ and G in the simulations exhibit the same characteristics as the model (6). In order to examine to what extent the model can quantitatively predict the orbit, we need to determine the values of a', b', and c' from the simulation results and then make a comparison between the two predictions. There are two methods for determining a' and b': one is to take a' as $\dot{\varphi}_{\max}$ and b' as $\dot{\varphi}_{\min}$, the other is to calculate them from G with (19). The two methods give the same results if the simulated orbit behavior are in perfect agreement with the model prediction (10) or (11). In the following, we only use the former to fit the model to the simulation results, just in order to assess the model.

A close scrutiny into Fig. 6 and the corresponding data show that the behavior of φ is not in perfect agreement with the model. One difference is that the inertial effect results in $\dot{\varphi}_{\min}$ occurring at an angle slightly less than $m\pi+\frac{\pi}{2}$, not precisely at $m\pi+\frac{\pi}{2}$. This behavior was also observed by Ding and Aidun [13] in their simulations of the rotation of an ellipse in simple shear flow. Figure 6 shows at $\mathrm{Re}_s=12.8$, both $\dot{\varphi}_{\min}$ and $\dot{\varphi}_{\max}$ in all periods are almost the same, being 0.762 and 0.182, respectively. We plot $\tan(\varphi)$ as a function of $\tan(\omega t+k')$ at $\mathrm{Re}_s=12.8$ in Fig. 8. It is clear that the result departs slightly away from the model prediction. As a result, it is not surprising that there are discrepancies between the periods obtained with the simulations and the model. The model gives the period of $2\pi/\sqrt{a'b'}\simeq16.9$ using $a'=0.762$ and $b'=0.182$, which is slightly larger than the simulation result of $T=16.6$.

Ding and Aidun [13] found that the rotation period of an elliptical cylinder in simple shear flow was proportional to $(\mathrm{Re}_{sc}-\mathrm{Re}_s)^{-1/2}$ at small $(\mathrm{Re}_{sc}-\mathrm{Re}_s)$ and they explained the result by two observations: one was that in the vicinity of φ^* where $\dot{\varphi}$ reached its minimum $\dot{\varphi}_{\min}$, $\dot{\varphi}\sim\dot{\varphi}_{\min}+B(\varphi-\varphi^*)^2$, B being a constant; the other was that $\dot{\varphi}_{\min}\sim(\mathrm{Re}_{sc}-\mathrm{Re}_s)$ at small $(\mathrm{Re}_{sc}-\mathrm{Re}_s)$. This result can be easily derived from our model by assuming $\dot{\varphi}_{\max}$ is independent of Re_s and $\dot{\varphi}_{\min}$ is proportional to $(\mathrm{Re}_{sc}-\mathrm{Re}_s)$, since the model gives $T=2\pi(\dot{\varphi}_{\max}\dot{\varphi}_{\min})^{-1/2}$. Figure 6 shows that $\dot{\varphi}_{\max}$ is not sensitive to Re_s, although it changes with time at relatively high Re_s. On the other hand, $\dot{\varphi}_{\min}$ approaches zero as Re_s increases. The relationship between $\dot{\varphi}_{\min}$ and Re_s is plotted in Fig. 9. For convenience, $\dot{\varphi}_{\min}$ is computed near $\varphi=\frac{3\pi}{2}$. From Fig. 6, $\dot{\varphi}_{\min}$ for different periods does not differ significantly at $\mathrm{Re}_s\leqslant192$. Accordingly, we calculate the periods using the data at $\pi\leqslant\varphi\leqslant2\pi$, and the result is shown in Fig. 10.

Figure 9 illustrates that at Re_s from 96 to 256, $\dot{\varphi}_{\min}$ decreases approximately linearly with increasing Re_s and can be fitted as $\dot{\varphi}_{\min}=4.424\times10^{-4}(289-\mathrm{Re})$. Simply setting $a'=0.7$ (see Fig. 6), we obtain $T=357(289-\mathrm{Re}_s)^{-1/2}$, which is found systematically a little larger than the periods obtained with the simulations, as demonstrated in Fig. 10.

Substituting $a'=0.7$ and $b'=4.424\times10^{-4}(289-\mathrm{Re}_s)$ into (18) yields the average amplitude $A=3-\ln(289-\mathrm{Re}_s)/2$. This result is compared to the simulation result in Fig. 11 and the model prediction is found systematically smaller than the simulation data. The comparison of the evolutions of $G(t)$ between the simulation at $\mathrm{Re}_s=38.4$ and the model prediction is given in Fig. 12. In the model, $a'=0.73$, $b'=0.138$, and $c'=0.0267$. We can see that apart from small differences in T and A, there is also a phase difference between the two

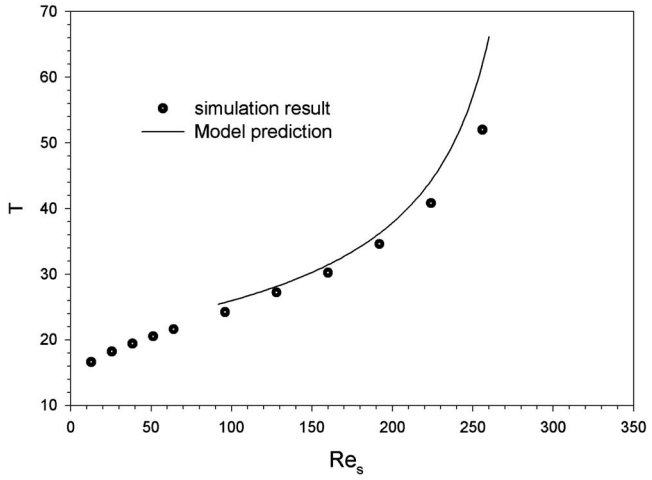

FIG. 10. The period T vs Re_s. For the simulation result, T is calculated from the data for $\varphi=\pi\sim2\pi$. For the model prediction, $a'=0.7$, $b'=4.424\times10^{-4}(289-\mathrm{Re}_s)$. $\theta_0=\frac{\pi}{4}$, $\varphi_0=\frac{\pi}{2}$.

results due to the fact that the spheroid does not start to rotate from a well-developed orbit, but from a zero angular velocity (see Fig. 6), and consequently there is a pronounced transient effect on the rotation of the spheroid at early times that was not captured adequately by the model.

The above method for determining a' and b' matches $\dot{\varphi}_{\min}$ and $\dot{\varphi}_{\max}$ between the simulation and the model. The other method (19) matches T and A. Due to the slight departure of the orbit characteristics of the spheroid in the simulations away from the model prediction, it is not possible to match all quantities. Since T and A are more important than $\dot{\varphi}_{\min}$ and $\dot{\varphi}_{\max}$ for the description of the rotation of the spheroid, it may be better to use the second method to determine a' and b' in the model if one wants to use the model to analyze the rotation of spheroids.

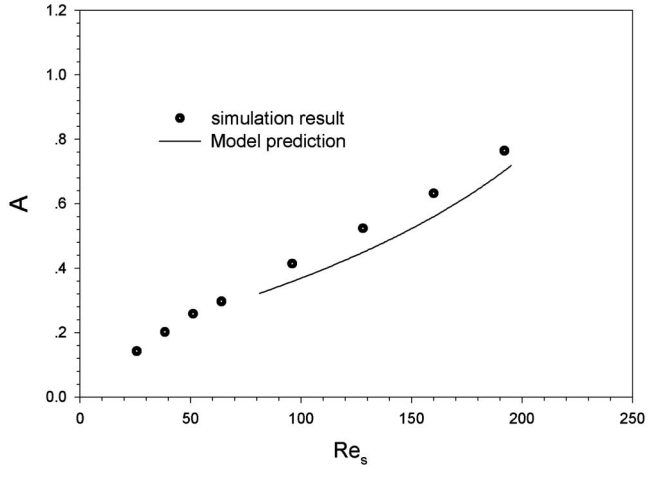

FIG. 11. The average amplitude A vs Re_s for a prolate spheroid, as compared to the model prediction. For the simulation result, A is calculated from $G(t)$ for $\varphi=\frac{3\pi}{2}-\frac{5\pi}{2}$. For the model prediction, $a'=0.7$, $b'=4.424\times10^{-4}(289-\mathrm{Re}_s)$. $\theta_0=\frac{\pi}{4}$, $\varphi_0=\frac{\pi}{2}$.

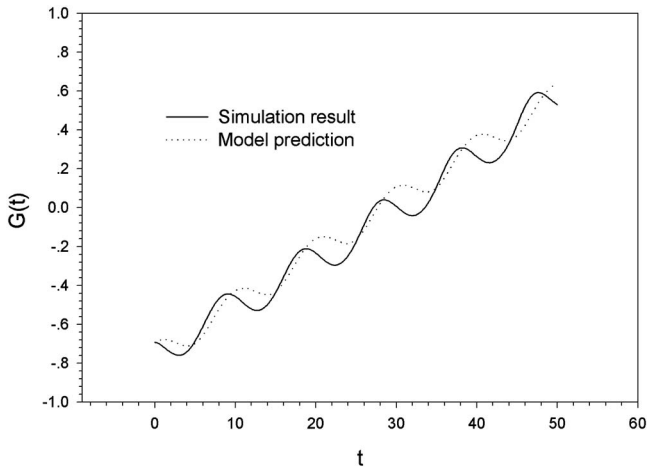

FIG. 12. Comparison of the evolutions of $G(t)$ between the simulation results at $\mathrm{Re}_s=38.4$ and the model. For the model, $a'=0.73$, $b'=0.138$, and $c'=0.0267$.

3. Effects of initial orientation

Comparison of Fig. 13 and Fig. 5 reveals that the growth rate c' is smaller at $\theta_0=\frac{\pi}{6}$ than at $\theta_0=\frac{\pi}{4}$ at the same Re_s. Figure 9 also shows that $\dot{\varphi}_{\min}$ is typically smaller at $\theta_0=\frac{\pi}{6}$ than at $\theta_0=\frac{\pi}{4}$ for the same Re_s. Re_{sc1} is about 160 for $\theta_0=\frac{\pi}{4}$, whereas it is less than 128 for $\theta_0=\frac{\pi}{6}$. As a result, there exist different steady states at a fixed Reynolds number. For example, at $\mathrm{Re}_s=128$, the steady state is log rolling for $\theta_0=\frac{\pi}{6}$, but tumbling for $\theta_0=\frac{\pi}{4}$. The effects of other initial orientations at $\mathrm{Re}_s=128$ are plotted in Fig. 14. It seems that the growth rate is lower at a smaller G_0, i.e., smaller θ_0 and φ_0 closer to $m\pi+\frac{\pi}{2}$.

We attribute the above bifurcation phenomenon (i.e., different steady states at a fixed Reynolds number depending on the initial condition) to the particle and fluid inertial effects. At a low Reynolds number, there is no bifurcation since the inertial effect is absent or very small and the rotation of the

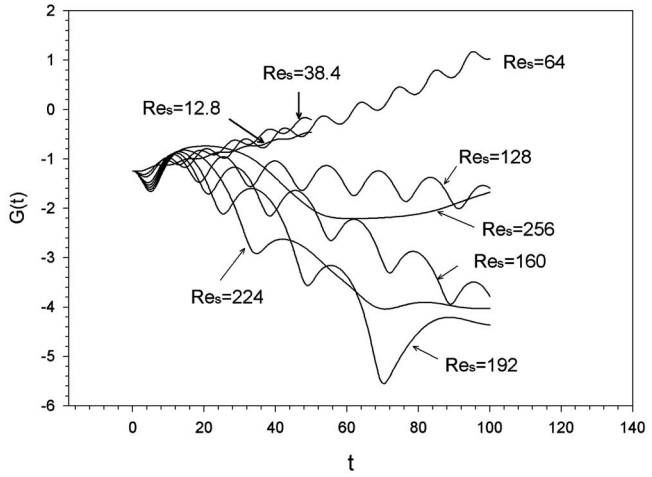

FIG. 13. The evolutions of the orbit function G at different Re_s. $\theta_0=\frac{\pi}{6}$, $\varphi_0=\frac{\pi}{2}$.

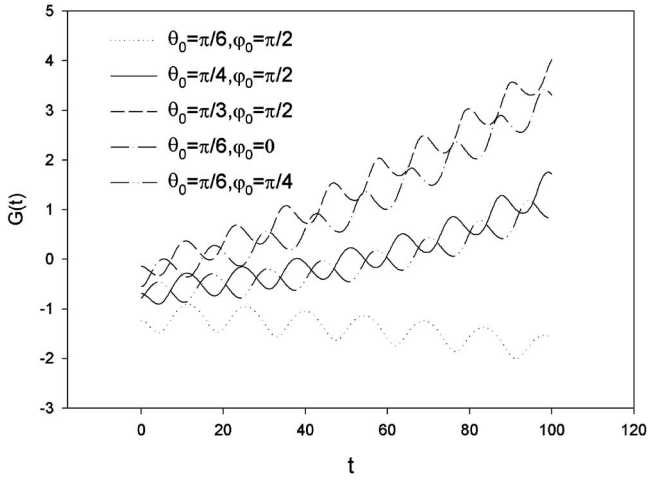

FIG. 14. The evolutions of the orbit function G at different initial orientations. $\mathrm{Re}_s=128$.

spheroid solely depends on the hydrodynamic force. By contrast, the particle inertia plays an important role in the motion of the spheroid at a high Reynolds number, and therefore the spheroid released from different orientations at initial time can follow different orientational orbits and reach different steady states.

C. Oblate case

We first examine the orbit behavior at a fixed initial orientation of $\theta_0=\frac{\pi}{4}$ and $\varphi_0=0$. For $\mathrm{Re}_s=0-192$, the numerical results indicate that there exist three Reynolds regimes for different steady states:

(i) Regime one ($0<\mathrm{Re}_s<\mathrm{Re}_{sc1}$). The oblate spheroid will eventually turn its axis of symmetry parallel to the vorticity axis. As shown in Fig. 15, the turning velocity for the oblate case is much higher than that for the prolate case at the comparable Re_s. Persistent rotation of the spheroid about the vorticity axis is observed at $\mathrm{Re}_s=12.8$ and $\mathrm{Re}_s=38.4$, and

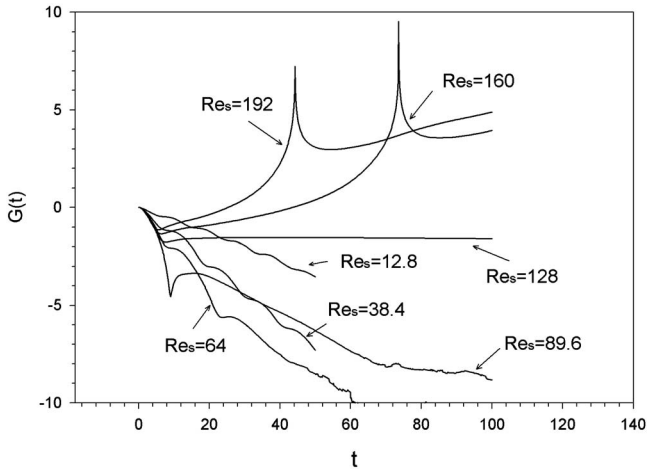

FIG. 15. The evolutions of the orbit function G at different Re_s for an oblate spheroid. $\theta_0=\frac{\pi}{4}$, $\varphi_0=0$.

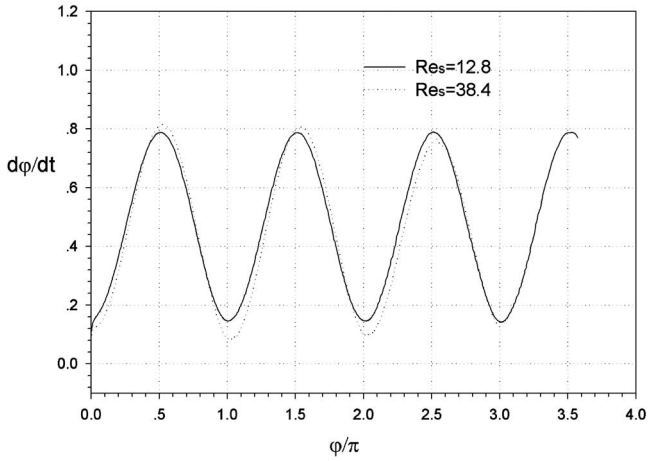

FIG. 16. $(d\varphi/dt)$ vs φ/π at $\mathrm{Re}_s=12.8$ and 38.4 for an oblate spheroid. $\theta_0=\frac{\pi}{4}$, $\varphi_0=0$.

Fig. 16 reveals that $\dot{\varphi}$ is a sinelike function of φ, still approximately satisfying the model prediction. $\dot{\varphi}_{\min}$ occurs at angles slightly larger than $m\pi$, and this is an anomalous behavior, because we have seen that the orientation of the broadside of the prolate spheroid is slightly less than $m\pi+\frac{\pi}{2}$, when $\dot{\varphi}$ reaches its minimum, and we will see that the fixed orientation of the broadside of the oblate spheroid is also slightly less than $m\pi+\frac{\pi}{2}$ when the oblate spheroid completely ceases its rotation about the vorticity axis at high Re_s (Fig. 18). Figure 17 shows that the regularly periodic rotations will stop at $\mathrm{Re}_s=64$ and $\mathrm{Re}_s=89.6$. For $\mathrm{Re}_s=64$, the rotation can pass through $\varphi=\pi$ and our data show $\dot{\varphi}_{\min}$ occurs at an angle larger than π. For $\mathrm{Re}_s=89.6$, the spheroid rotates back soon after its release and stays at the orientation of φ slightly smaller than zero for a long time. The orientation data of the spheroids at $t>60$ for both $\mathrm{Re}_s=64$ and $\mathrm{Re}_s=89.6$ shown in Fig. 17 may not be reliable because at that time p_x and p_y are too small (see Fig. 15).

(ii) Regime two ($\mathrm{Re}_{sc1}<\mathrm{Re}_s<\mathrm{Re}_{sc2}$). When Re_s increases up to 128, the spheroid will not align its axis with the vor-

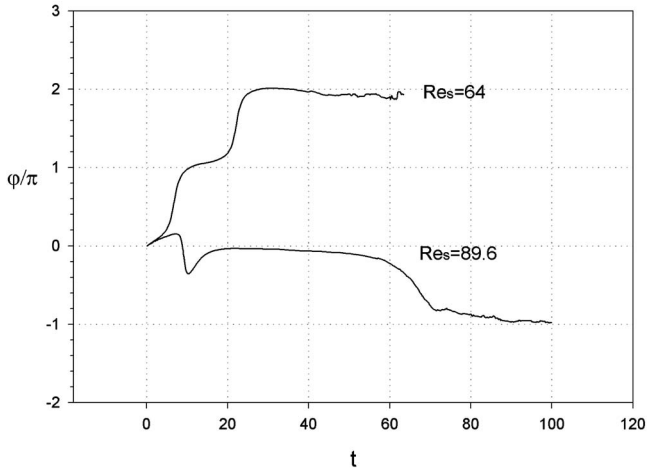

FIG. 17. The evolutions of φ/π at $\mathrm{Re}_s=64$ and 89.6 for an oblate spheroid. $\theta_0=\frac{\pi}{4}$, $\varphi_0=0$.

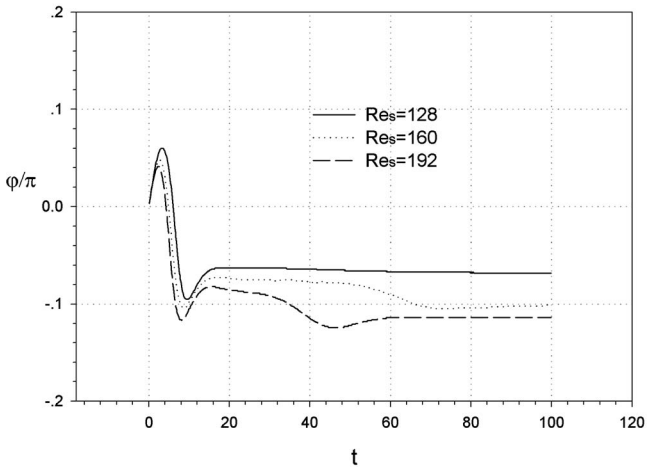

FIG. 18. The evolutions of φ/π at $\mathrm{Re}_s=128$, 160, and 192 for an oblate spheroid. $\theta_0=\frac{\pi}{4}$, $\varphi_0=0$.

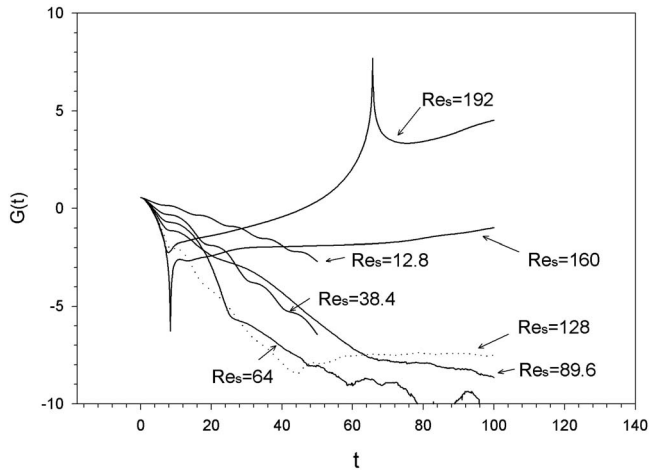

FIG. 20. The evolutions of the orbit function G at different Re_s for an oblate spheroid. $\theta_0=\frac{\pi}{3}$, $\varphi_0=0$.

ticity axis, but stays almost in the gradient-vorticity plane (φ is about -0.06π, from Fig. 18), with θ between 0 and $\frac{\pi}{2}$. This is the state of "inclined rolling." It is difficult to determine the subcritical and supercritical Reynolds numbers Re_{sc1} and Re_{sc2}, since G or θ cannot be calculated accurately when the spheroid axis is very close to the vorticity axis or the flow-gradient plane. For example, it is difficult to discern if $\mathrm{Re}_s=89.6$ belongs to the log-rolling regime or the inclined-rolling regime, based on the result in Fig. 15 and in Fig. 19. It may be more suitable to define a critical G or θ threshold for demarcating this regime. Figures 15 and 19 show that the Reynolds number interval for an obvious inclined-rolling state is small, and is expected to be much narrower than (89.6,160).

(iii) Regime three ($\mathrm{Re}_s>\mathrm{Re}_{sc2}$). In this regime, the oblate spheroid will turn its axis of symmetry parallel to the gradient axis along approximately the gradient-vorticity plane. Figure 18 shows that the deviation of the orientation φ from the gradient axis ($m\pi$) increases with increasing Re_s, consistent with the results of Ding and Aidun [13] for the ellipse case. In addition, Fig. 19 indicates that there is an overshoot for the spheroid approaching the flow-gradient plane, resulting in a striking pulse of G in Fig. 15.

Therefore, with the shear Reynolds number increasing from zero to 192, the rotation of an oblate spheroid undergoes the following transitions: Jeffery orbit, log rolling, inclined rolling, and motionless state. The log-rolling and inclined-rolling states have also been identified by Qi and Luo [15,16].

The results of G at $\theta_0=\frac{\pi}{3}$ and $\varphi_0=0$ are shown in Fig. 20. Like the prolate case, the behavior of G also depends on the initial orientations of the spheroid. The significant effects of the initial orientations occur at Re_s being 128 and larger. In this high Re_s regime, it appears that the axis of the spheroid for $\theta_0=\frac{\pi}{3}$ can approach closer to the vorticity axis and then the turning of the axis of the spheroid away from the vorticity axis is hindered, compared to the case of $\theta_0=\frac{\pi}{4}$ (Figs. 15 and 20). Again, at $\mathrm{Re}_s=128$, there exist two steady states: log rolling for $\theta_0=\frac{\pi}{3}$ and inclined rolling for $\theta_0=\frac{\pi}{4}$.

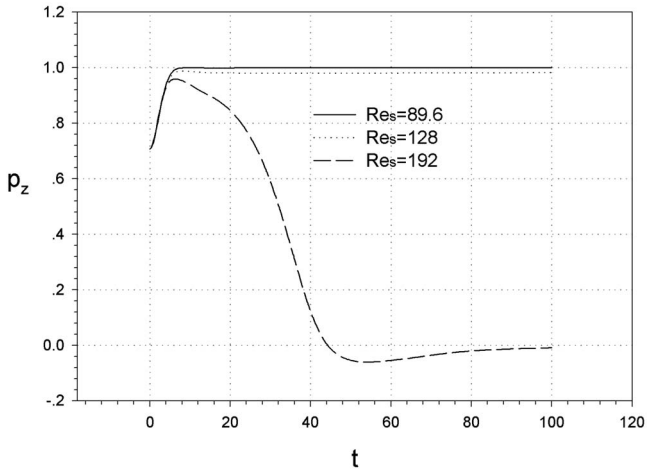

FIG. 19. The evolutions of p_z at $\mathrm{Re}_s=128$, 160, and 192 for an oblate spheroid. $\theta_0=\frac{\pi}{4}$, $\varphi_0=0$.

IV. CONCLUSIONS

We have presented the DLM/FD algorithm for the simulation of the motion of three-dimensional nonspherical particles in fluids and a simple empirical model for the description of the rotation of a spheroid in simple shear flow (and possibly other types of flows). The numerical results on the rotation of both prolate and oblate spheroids in a Couette flow have been reported and compared to the empirical model. The following conclusions can be drawn from the present study:

(1) When the effects of inertia are not too strong to cause the stop of the rotation of the spheroid axis about the vorticity axis, $\dot{\varphi}$ is approximately a cosine function of φ and the

exponential grow rate of the orbit function c' is approximately a constant. These two characteristics of the orbit can be well predicted by a simple model.

(2) For a fixed initial orientation, with Re_s increasing from 0 to 256, the steady states for a prolate spheroid undergo the following transitions: Jeffery orbit, tumbling, quasi-Jeffery orbit, log rolling, and inclined rolling.

(3) For a fixed initial orientation, with Re_s increasing from 0 to 192, the steady states for an oblate spheroid undergo the following transitions: Jeffery orbit, log rolling, inclined rolling, and motionless state.

(4) The orbit behavior is significantly affected by the initial orientation. There exist different steady states for certain shear Reynolds number regimes.

ACKNOWLEDGMENTS

The authors wish to thank Professor Xijun Fan for helpful discussions about the empirical model. The work is mainly based on a part of the thesis work of one of the authors (Z.Y.) at the University of Sydney.

[1] G. B. Jeffery, Proc. R. Soc. London, Ser. A **102**, 161 (1922).
[2] F. P. Bretherton, J. Fluid Mech. **14**, 284 (1962).
[3] E. Y. Harper and I.-D. Chang, J. Fluid Mech. **33**, 209 (1968).
[4] L. G. Leal, J. Fluid Mech. **69**, 305 (1975).
[5] O. G. Harlen and L. L. Koch, J. Fluid Mech. **252**, 187 (1993).
[6] Y. Iso, D. L. Koch, and C. Cohen, J. Non-Newtonian Fluid Mech. **62**, 115 (1996).
[7] N. Phan-Thien and X. J. Fan, J. Non-Newtonian Fluid Mech. **105**, 131 (2002).
[8] Y. Iso, C. Cohen, and D. L. Koch, J. Non-Newtonian Fluid Mech. **62**, 135 (1996).
[9] P. G. Saffman, J. Fluid Mech. **1**, 540 (1956).
[10] A. Karnis, H. L. Goldsmith, and S. G. Mason, Can. J. Chem. Eng. **44**, 181 (1966).
[11] J. Feng and D. D. Joseph, J. Fluid Mech. **303**, 83 (1995).
[12] D. Broday, M. Fichman, M. Shapiro, and C. Gutfinger, Phys. Fluids **10**, 86 (1998).
[13] E.-J. Ding and C. K. Aidun, J. Fluid Mech. **423**, 317 (2000).
[14] C. M. Zettner and M. Yoda, J. Fluid Mech. **442**, 241 (2001).
[15] D. W. Qi and L. S. Luo, Phys. Fluids **14**, 4440 (2002).
[16] D. W. Qi and L. S. Luo, J. Fluid Mech. **477**, 201 (2003).
[17] R. Glowinski, T.-W. Pan, T. I. Hesla, and D. D. Joseph, Int. J. Multiphase Flow **25**, 755 (1999).
[18] Z. Yu, N. Phan-Thien, and R. I. Tanner, J. Fluid Mech. **518**, 61 (2004).
[19] F. P. Folgar and C. L. Tucker, J. Reinf. Plast. Compos. **3**, 98 (1984).
[20] X. J. Fan, Ph.D. dissertation, University of Syndey, 2006.
[21] D. C. Rapaport, *The Art of Molecular Dynamics Simulation* (Cambridge University Press, Cambridge, 1995).
[22] Z. Yu, N. Phan-Thien, Y. Fan, and R. I. Tanner, J. Non-Newtonian Fluid Mech. **104**, 87 (2002).
[23] Z. Yu, Ph.D. dissertation, University of Sydney, 2003.